Journal of Molecular Catalysis A: Chemical 304 (2009) 28–32

Contents lists available at ScienceDirect

Journal of Molecular Catalysis A: Chemical

journal homepage: www.elsevier.com/locate/molcata

Effects of pH on hydrothermal synthesis and characterization of visible-light-driven $BiVO_4$ photocatalyst

Aiping Zhang*, Jinzhi Zhang, Naiyi Cui, Xiaoyun Tie, Yanwei An, Lingjie Li

College of Sciences, North China University of Technology, No. 5 Jinyuanzhuang Road, Beijing 100144, People's Republic of China

ARTICLE INFO

Article history:
Received 16 October 2008
Received in revised form 14 January 2009
Accepted 14 January 2009
Available online 21 January 2009

Keywords:
Bismuth vanadate
Visible-light-driven photocatalyst
Hydrothermal synthesis

ABSTRACT

$BiVO_4$ powders were hydrothermally synthesized at different pHs and characterized by XRD, SEM, DRS, nitrogen adsorption and Raman techniques. It revealed that the pH values of the precursors can influence significantly on the morphologies and structures of the products. The photocatalytic activities of the catalyst obtained were evaluated by the decolorization of methyl orange in aqueous solution under visible light irradiation. It was found that monoclinic $BiVO_4$ showed better photocatalytic activities than those shown by the tetragonal phase under visible light, which are attributed to its wider bandgap. The results also revealed that the dispersive particles with larger surface area represented higher activities than the coagulate ones when considering their photocatalysis.

1. Introduction

Since photocatalysis is regarded world-wide as one of the most promising solutions to solve the severe problems of energy shortage and environmental crisis, the development of visible-light-driven photocatalysts has been attracting much attention [1–3]. In the past decades, the interests of researchers in the application of photocatalysts have grown dramatically, which mainly involved the selective synthesis of efficient visible-light-driven photocatalysts, the photocatalysis mechanism and the effect factors about the degradation of organic contaminants, etc. [4–7].

As one of the non-titania based semiconductor photocatalysts, bismuth vanadate ($BiVO_4$) has recently attracted considerable attention for its strong photocatalysis for water splitting and pollutant decomposing under visible light irradiation [5]. Up until now, many methods for the preparation of $BiVO_4$, such as solid-state reaction, sol–gel method, coprecipitation and metalorganic decomposition, etc., have been reported [8–10]. There are three crystalline phases reported for synthetic $BiVO_4$, that is, the monoclinic sheelite-type, the tetragonal sheelite-type and the tetragonal zircon-type [9]. All the three crystal structures are well formed and are found to have tetrahedral V, which is coordinated by four oxygens, with Bi eightfold coordinated [11]. Although their photocatalytic properties are strongly related to their crystal structures and morphology [12], only limited researches have been done on the phase selectivity and associated catalytic activities under different synthetic conditions.

This study reported a hydrothermal route for selective synthesis of the highly crystalline $BiVO_4$ powders with high efficiency. For comparison, the pHs of the precursor mixtures were pre-set to different values. All the synthetic samples, which showed different photocatalytic activities, were characterized and compared using XRD, SEM, DRS, nitrogen adsorption and Raman techniques.

2. Experimental

2.1. Materials and synthesis of bismuth vanadate

Bismuth nitrate pentahydrate ($Bi(NO_3)_3{\cdot}5H_2O$) and Ammonium metavanadate (NH_4VO_3) supplied from Beijing Chemical Company were used directly without any further purification. Other chemicals used were all analytical grade. Solutions were prepared using deionized water. In a typical preparation, 0.02 mol $Bi(NO_3)_3{\cdot}5H_2O$ and 0.02 mol NH_4VO_3 were dissolved in 20 mL of 65% (w/w) HNO_3 and 20 mL 6 mol/L NaOH solutions separately, and each stirred for 2 h at room temperature. After that, these two mixtures were mixed together in 1:1 molar ratio and stirred for about 1 h to get a stable, salmon pink homogeneous solution. The diluted NaOH and HNO_3 solutions were then added for adjusting the pH value, which was taken to be 1.7, 3.2, 5.3, 6.9, 8.8 and 11.5. Mixture of each precursor were then sealed in a 50-ml Teflon-lined stainless autoclave and heated to 180 °C for 6 h under autogenous pressure. Afterwards, the precipitate was filtered, washed with distilled water three times for each, and dried in vacuum at RT for 12 h.

* Corresponding author. Tel.: +86 10 88803271; fax: +86 10 88803271.
E-mail address: ncutalex@126.com (A. Zhang).

1381-1169/$ – see front matter © 2009 Elsevier B.V. All rights reserved.
doi:10.1016/j.molcata.2009.01.019

2.2. Apparatus and measurements

X-ray powder diffraction (XRD, Puxi Co. Ltd., model XD-3) data were recorded in the region of $2\theta = 10–65^\circ$ using a Cu Kα radiation ($\lambda = 0.15418$ nm) with a scan step of 2.0°/min at RT with a counter diffractometer. The morphologies and microstructures of the as-prepared samples were examined using scanning electron microscopy (SEM, Hitachi, model S-3500N). The optical-absorbance of the samples were analyzed using a doubled-beam UV–visible spectrophotometer (Puxi Co. Ltd., model TU-1901) equipped with an integrating sphere. The UV–vis diffusion reflectance spectra (DRS) of $BiVO_4$ were recorded with $BaSO_4$ as a reference and were converted from reflection to absorbance by Kubelka–Munk method [13]. The Raman spectra was recorded by a Raman microprobe system (Renishaw, model H13325), with a 514.5-nm Ar-ion laser source used for excitation. Nitrogen adsorption–desorption measurements were conducted at 77.35 K on a Micromeritics Tristar 3000 analyzer after samples were degassed at 200 °C for 4 h. The Brunauer–Emmett–Teller (BET) surface area was estimated using adsorption data in a relative pressure range from 0.05 to 3.0.

2.3. Photocatalytic activity test

Photocatalytic activities of the samples were determined by the decolorization of methyl orange (MO) under visible light irradiation. A 500-W Xe-illuminator was used as a light source and set about 10 cm apart from the reactor. The 420 nm cutoff filter was placed between the Xe-illuminator and the reactor to completely remove all incoming wavelengths shorter than 420 nm to provide visible light irradiation. Experiments were carried out at ambient temperature as follows: the same amount (0.2 g) of photocatalyst was added into 100 mL of 10 mg/L MO solution. Before illumination, the solution was stirred for 10 min in darkness in order to reach the adsorption–desorption equilibrium for MO and dissolved oxygen. At different irradiation time intervals, about 5 mL suspensions were collected, and then centrifugalized to remove the photocatalyst particles. The concentrations of the remnant MO were monitored in the way of checking the absorbance of solutions at 464 nm during the photodegradation process.

3. Results and discussion

3.1. Powder formation

The hydrothermal treatment for the precursor mixtures always leads to highly crystalline samples. Fig. 1 shows the XRD patterns of the prepared samples as a function of pH values. For the samples synthesized at pH = 11.5 and 8.8, the diffraction data obtained match well with those for the monoclinic $BiVO_4$ (JCPDS card no. 14-0688). As can be seen from Fig. 1f and e, no peaks of any other phases or impurities were detected. As the pH decreases to 5.3 (Fig. 1c), the peaks for the tetragonal $BiVO_4$ (JCPDS card no. 14-0133) appear along with those for the monoclinic type, indicating that this sample is a mixture of tetragonal and monoclinic $BiVO_4$. The difference in the XRD patterns between tetragonal and monoclinic $BiVO_4$ can be judged mainly by (1) the existence of peaks (2 0 0) and (1 2 1) and (2) the existence of a peak at 15° and the splitting of peaks at 18.5° and 35°. As the pH values decreased from 5.3 to 3.2 (Fig. 1b), the peaks corresponding to tetragonal $BiVO_4$ became stronger and stronger whereas the peaks assigned to monoclinic type decreased. The percentage of the monoclinic phase has been calculated based on the normalized ration of relative intensities for the (1 2 1) peak of monoclinic phase against that for the (2 0 0) peak of the tetragonal phase, i.e.

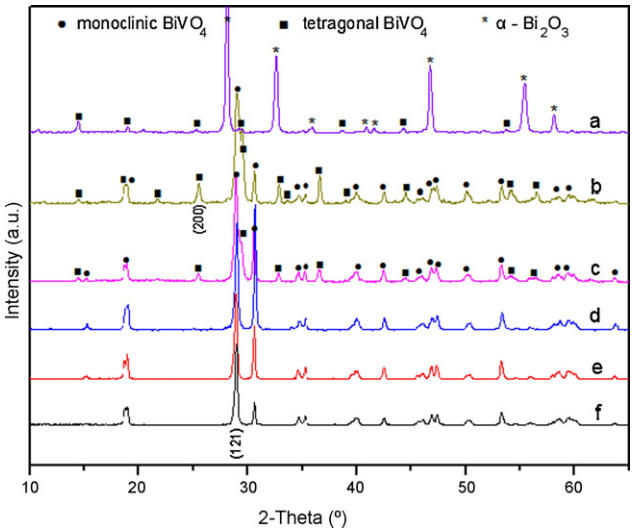

Fig. 1. The XRD pattern of powders prepared at different pHs: (a) 1.7; (b) 3.2; (c) 5.3; (d) 6.9; (e) 8.8; (f) 11.5. The dark circles and squares indicate the peaks representing the monoclinic and tetragonal forms of $BiVO_4$, respectively; and asterisk denote α-Bi_2O_3 phase.

$$\eta_{\text{mono}} = \frac{I_{\text{mono}(1\,2\,1)}}{I_{\text{mono}(1\,2\,1)} + I_{\text{tetra}(2\,0\,0)}} \quad (1)$$

where η_{mono}, $I_{\text{mono}(1\,2\,1)}$ and $I_{\text{tetra}(2\,0\,0)}$ denote the percentage of the monoclinic phase, the relative intensity of the (1 2 1) peak for the monoclinic phase and that of the (2 0 0) peak for the tetragonal phase, respectively. The relationship between pH and the calculated percentage of the monoclinic phase is shown in Table 1.

When the pH value decreased to 1.7 (Fig. 1a), strong characteristic peaks associated with the α-Bi_2O_3 (JCPDS card no. 27-0052) [14] and the trace of $BiVO_4$ (only tetragonal type) were both observed. This can be attributed to the loss of vanadium precursor via volatilization. On the basis of this synthesis route, the relevant chemical reactions can be formulated as follows [15],

$$Bi(NO_3)_3 + H_2O \Leftrightarrow 2HNO_3 + BiONO_3 \quad (2)$$

$$BiONO_3 + VO_3^- \Leftrightarrow BiVO_4 + NO_3^- \quad (3)$$

Table 1
pH values of homogeneous precursor mixtures, bandgaps (E_g), BET surface areas, percentage of monoclinic $BiVO_4$ powders (η_{mono}), final conversion rate (D) and degradation rate constant (k) of dyes.

Item	Sample					
	(a)	(b)	(c)	(d)	(e)	(f)
pH values of precursor	1.7	3.2	5.3	6.9	8.8	11.5
E_g (eV)	2.92	2.83	2.75	2.29	2.40	2.51
A_{BET} ($m^2\,g^{-1}$)	4.21	4.08	4.43	4.98	2.33	1.86
η_{mono} (%)	0	74.4	83.3	98.7	100	100
D (%) = $(C_0 - C)/C_0 \times 100$	17.4	41.5	49.7	98.5	89.9	78.8
Degradation rate constant k (min^{-1})	0.0021	0.0031	0.0039	0.0088	0.0075	0.0068

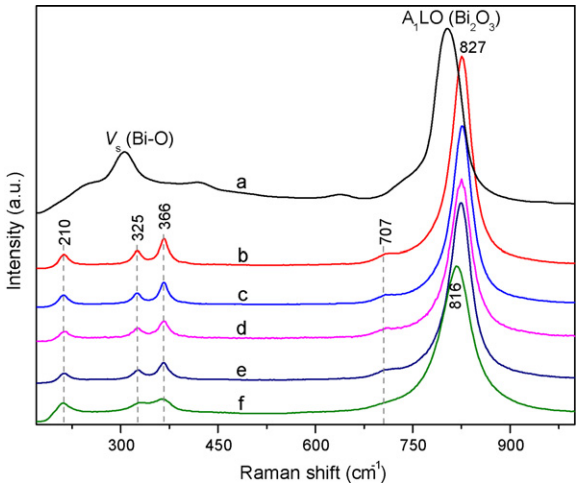

Fig. 2. Raman spectra of samples prepared at different pHs: (a) 1.7; (b) 3.2; (c) 5.3; (d) 6.9; (e) 8.8; (f) 11.5.

Initially, the reactants were dissolved in concentrated HNO_3 and no precipitate could be found. As the pH decreased, $Bi(NO_3)_3$ reacted gradually with water to form slightly soluble $BiONO_3$, as shown in formula (2). And then, the newly formed $BiONO_3$ reacted with VO_3^-, forming a yellow $BiVO_4$ as shown in formula (3). Although the monoclinic $BiVO_4$ is thermodynamically more stable than tetragonal $BiVO_4$ at room temperature, the formation of the tetragonal $BiVO_4$ seems to be more feasible kinetically by a sudden decrease in pH of precursor [8,15]. This suggests that the dissolution and the subsequent recrystallization occurring in the low pH solution contribute to the phase transformation of the monoclinic type into the tetragonal type. As indicated by formula (2), the addition of HNO_3 to the precursor mixtures halts the production of $BiONO_3$ from $Bi(NO_3)_3$. Meanwhile, the following hydrothermal treatment may lead to the loss of vanadium via vitalization and the decomposition of $Bi(NO_3)_3$. Thus, the strong peaks of Bi_2O_3 found dominate obviously in the whole XRD pattern with only amount of tiny remnant $BiVO_4$ presented.

Based on the XRD results obtained, it can be deduced that high pH (>7) is sufficient for the formation of the monoclinic $BiVO_4$ powder from NH_4VO_3 and $Bi(NO_3)_3$, and pure phase monoclinic $BiVO_4$ can be selectively synthesized by simply adjusting the preparation pH values of solutions using hydrothermal treatment. However, a set of $BiVO_4$ samples prepared by the same aging with pH adjustment but without hydrothermal treatment showed large diameter scale; and all the $BiVO_4$ samples were composed of both monoclinic and tetragonal phases according XRD results.

3.2. Morphologies and structures performance

The identity of the constituent of $BiVO_4$ in the samples was confirmed by Raman spectra, which are presented in Fig. 2 and Table 2. It shows features similar to those reported previously [16,17]. The spectra are dominated by an intense band near 820 cm^{-1}, assigned to the symmetric V–O stretching mode (A_g symmetry), and a weak shoulder located at about 707 cm^{-1} is assigned to the anti-symmetric V–O stretching mode (B_g symmetry). The symmetric (A_g) and the anti-symmetric (B_g) bending modes of vanadate anion are found at 366 and 325 cm^{-1}, respectively. The external modes (rotation/translation) were recorded at 210 cm^{-1}. The positions and the full width at half maximum (FWHM) of the most intensive bands near 820 cm^{-1} were determined using Lorentzian-type curve fitting. A gradual shift of these Raman bands towards the lower end of wavenumber, i.e., from 827 to 816 cm^{-1}, reveals that the average short-range symmetry of the VO_4 tetrahedra becomes more regular [4,18]. On the contrary, the values of FWHM increase by the same order. It is known that Raman band positions are very sensitive to the short-range order whereas the Raman widths are more sensitive to the degree of crystallinity, defects and disorders, particle size and/or aggregation of particles. Therefore, the Raman results indicate that the samples prepared at high pH values consisted VO_4 tetrahedra of less symmetric than those prepared at low pHs. The higher pH samples were of better crystallinity and contained lesser defects than samples prepared at lower pH conditions.

Fig. 3 shows the SEM micrographs of the powder samples prepared at different pHs. It is seen obviously that pH value can significantly influence on the sample morphology. As shown in Fig. 3a, both acicular and plate-like particles, synthesized at pH = 1.7, possess small particle sizes and smooth surface with some of them clustered into aggregates. The $BiVO_4$ sample (b), synthesized at pH = 3.2, is composed of aggregates of small crystals (seen in Fig. 3b). Differently, the sample synthesized at a higher pH (5.3) showed a few slice-like shape particles and most morphologically large-size aggregates. SEM image suggests that each aggregate was yielded from a common slice with a layered flower-like pattern, thus led to the disheveled figuration in Fig. 3c. For the samples prepared at pH = 6.9, rod- and slice-like grains can be seen in Fig. 3d. The different shapes of this sample may be from the sintering effect of crystals in a one-dimensional fashion, because some shorter rods and smaller slices were also observed in the images. Seen from Fig. 3e, large agglomerations adhered by many primary particles on the whole surface were expressed when synthesized at pH = 8.8. In contrast, the samples prepared at pH = 11.5 were obtained with more crystal-like shape for each particles (see Fig. 3f). Although each particle still had small size, they were significantly sintered to each other to form a large agglomeration. Their specific surface areas of the different samples are summarized in Table 1. It was found that their specific surface areas of samples are all high, which indicate that there would be high activities considering their photocatalysis.

The UV–vis diffuse reflectance spectra (DRS) of samples are shown in Fig. 4. It was found that these samples showed a new variation absorption in visible light region in addition to that strong absorption in the UV light region. The steep shape of the spectra indicated that the visible light adsorption was due to the bandgap transition. The absorption band contains a tail extending rightwards until about 600 nm. This may result from the crystal defects formed during the growth of $BiVO_4$. It is well known that the electronic structure of the semiconductor usually plays a crucial role in

Table 2
Assignation of Raman wavenumber observed for samples obtained by hydrothermal method.

Sample (b)	Sample (c)	Sample (d)	Sample (e)	Sample (f)	Assignation
827(41)	824(45)	822(48)	821(53)	816(64)	ν_s(V–O) (FWHM)
707	707	707	707	707	ν_{as}(V–O)
366	366	366	366	366	$\delta_s(VO_4^{3-})$
325	325	325	325	325	$\delta_{as}(VO_4^{3-})$
210	210	210	210	210	External mode

Note: ν_s: symmetric stretching mode; ν_{as}: asymmetric stretching mode; δ_s: symmetric deformation mode; δ_{as}: asymmetric deformation mode.

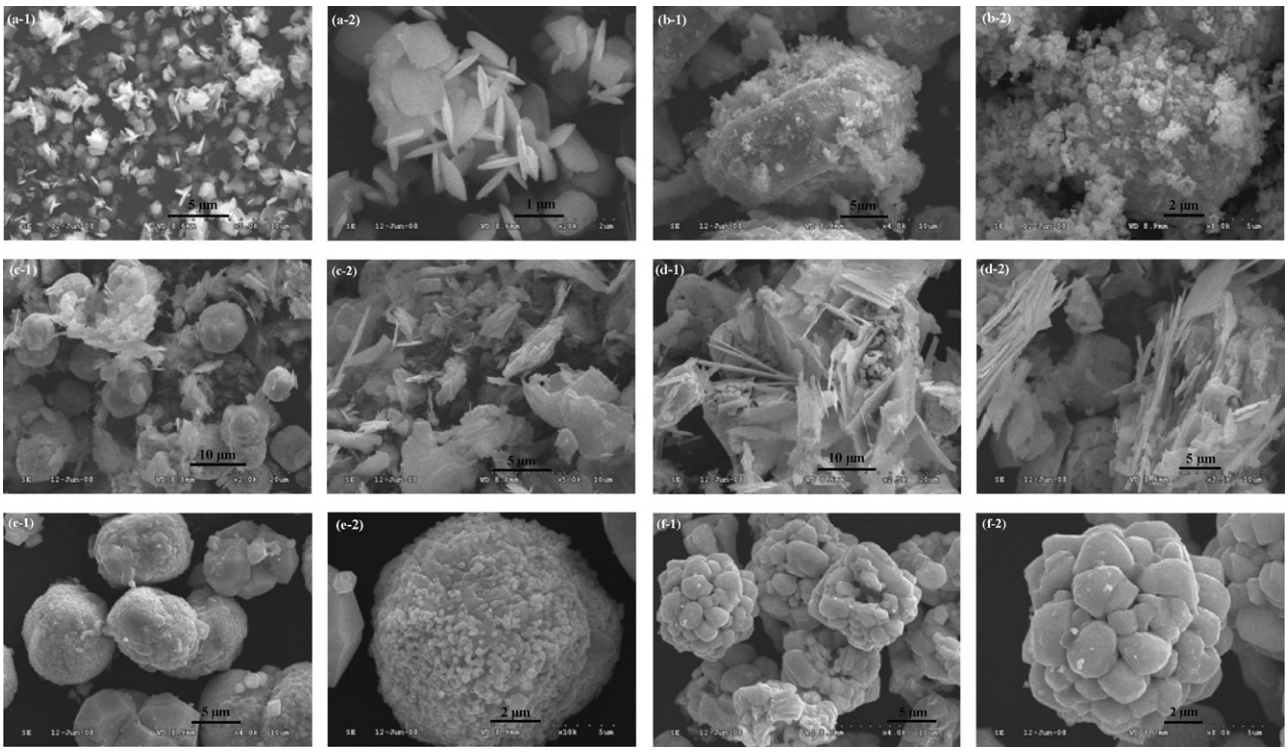

Fig. 3. SEM micrographs of powder samples prepared at different pHs: (a) 1.7; (b) 3.2; (c) 5.3; (d) 6.9; (e) 8.8; (f) 11.5.

its photocatalytic activity. The DFT calculations of electronic structure suggested that the valence band (VB) of $BiVO_4$ is formed by hybridized Bi 6s and O 2p orbitals, whereas the conduction band (CB) is formed by V 3d orbitals [19]. The hybridization of the Bi 6s and O 2p orbital makes the VB largely extended which hence increases the mobility of photo-excited holes and thus favors the photocatalytic oxidation of organic pollutants [20]. It was found that the tetragonal $BiVO_4$ with a 2.9 eV bandgap causes an absorption band mostly in the UV region while the monoclinic $BiVO_4$ with a 2.4-eV bandgap had a characteristic visible light absorption band in addition to the UV band [21].

The bandgap-widths of samples were calculated from the DRS. By extrapolation of the onset of the rising part to the *x*-axis (λ_g, nm) in the plots (as shown in Fig. 4 by the dotted line), the bandgap (E_g, eV) was determined from equation $E_g = 1240/\lambda_g$. The absorption edges of samples shifts with the increase of pH from about 430 to 540 nm. Thus the bandgap energy can be estimated to be about 2.92, 2.83, 2.75, 2.39, 2.43 and 2.51 eV for samples prepared at pH = 1.7, 3.2, 5.3, 6.9, 8.8 and 11.5, respectively. These data agrees with their components and clearly demonstrates that the electronic structures of samples were changed with the pH used in the hydrothermal synthesis.

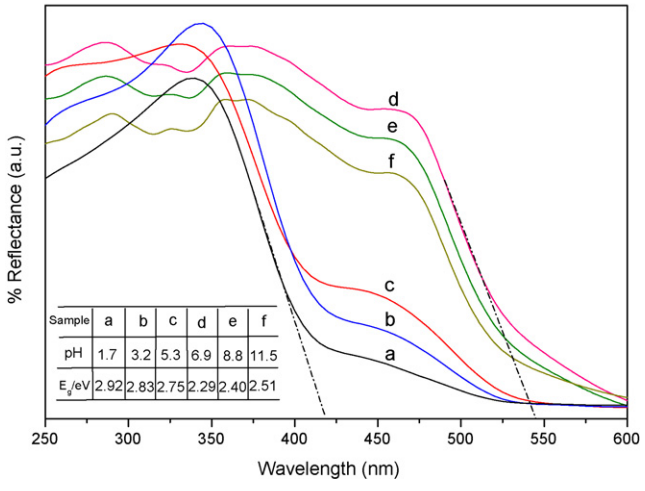

Fig. 4. Visible reflectance diffusion spectra for samples prepared at different pHs: (a) 1.7; (b) 3.2; (c) 5.3; (d) 6.9; (e) 8.8; (f) 11.5.

3.3. Photocatalyis activities

Azobenzene organic dye methyl orange with a major absorption band at about 464 nm was chosen as a model compound to study the photocatalytic activities of the samples. As shown in the inset of Fig. 5, the 464 nm absorption band of the MO solutions decreased gradually during the photodegradation caused by as-prepared samples. The corresponding plot for the photodegradation rate of samples is also shown in Fig. 5, which is represented by the MO concentration as a function of irradiation time for different catalysts. As can be seen from the figure, the best photodegradation rate can be up to 98% in 60 min under visible light irradiation. When the initial concentration of dye is low, the pseudo-first order approximation given by Eq. (4) can be used to obtain a quantitative understanding of the reaction rates of the MO degradation [22],

$$\ln\left(\frac{C_0}{C}\right) = kt \tag{4}$$

where C_0 and C are the concentrations of dye in the solution before irradiation and after it is irradiated for t min, respectively. And k is the pseudo-first order rate constant. According to Eq. (4), the pseudo-first order rate constant k for the as-prepared samples has been calculated and listed in Table 1. This quantity is found to show the same scalar level among these samples though the difference is more than four times between the best and the worst when considering this pseudo-first order rate constant.

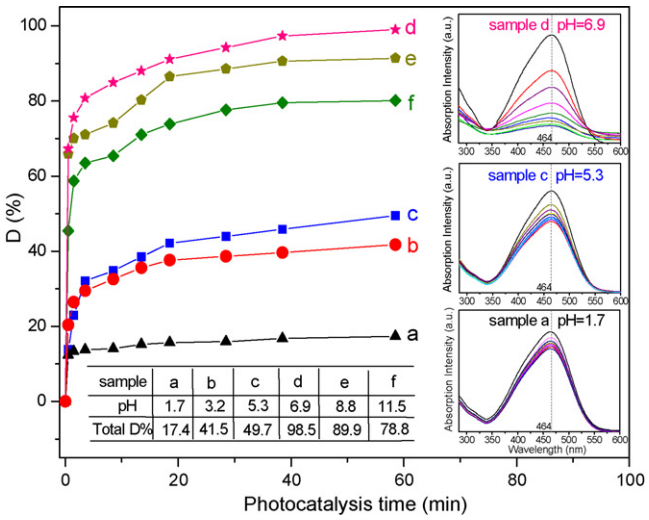

Fig. 5. Comparison of conversion activities between $BiVO_4$ samples prepared at different pHs: (a) 1.7; (b) 3.2; (c) 5.3; (d) 6.9; (e) 8.8; (f) 11.5. Here $D(\%) = (C_0 - C)/C_0 \times 100$, where C_0 is the initial MO concentration and C is the concentration after equilibrium adsorption.

The primary factors that influence a photocatalytic reaction are mainly: (1) the adsorption ability of the reactant on the catalyst surface, (2) the absorption ability of the catalyst used energy region of the light available, and (3) the efficient separation and transport of light-induced electrons and holes in the catalyst. The high photocatalytic activities of most samples examined can be attributed to the effective visible absorption and the relatively large surface areas of as-prepared $BiVO_4$.

The change in the electronic structures led to different degrees of delocalization of photogenerated electron–hole pairs, which therefore always leads to change in photocatalytic activity. As can be seen from Fig. 5d to c, the photocatalytic activity of the powders was decreased drastically associated with the phase transition from the monoclinic to the tetragonal $BiVO_4$. The reason probably is that recombination of the photogenerated electrons and holes are intensely suppressed in wide-bandgap monoclinic $BiVO_4$ in comparison to tetragonal type. The enhanced photocatalytic degradation of MO by sample (d) can be attributed not only to the strong absorption of visible light due to the bandgap, but also to the large surface area of particles which can easily adsorb MO molecules.

Most of the surface areas in the composite samples are large than pure monoclinic $BiVO_4$ samples based on BET analysis. And their photocatalytic activity was weakened heavily as the percentage of the tetragonal type increased. This may indicate that the type of crystal affects the photocatalytic activity predominantly in these samples. However, the activity was also decreased with the surface area decreased from sample (e) to sample (f), which indicate that the surface area plays an effective role on their photocatalysis (Fig. 5e and f). In addition, the BET surface area of sample (d) was estimated to be ca. 4.98 $m^2\,g^{-1}$, which was much higher than sample (e) of about 2.33 $m^2\,g^{-1}$. This large difference between their surface areas may influence their photocatalytic activities much, although these two samples represent almost the same crystalline phases and compositions. It can be generally concluded that the activity of a photocatalyst is determined not only by the specific surface area associated with their diameter and morphology, but also by the efficiency of the electron–hole separation correlated with their crystal/phase type.

4. Conclusion

A facile hydrothermal route for the synthesis of the visible-light-driven $BiVO_4$ photocatalyst at different pH conditions has been studied. The results showed that pH values of precursors strongly affected the structure and morphology of powders. The powder prepared at low pH contained mixed phase including monoclinic and tetragonal $BiVO_4$. With the increase of pH, a pure phase monoclinic type $BiVO_4$ could be synthesized selectively. Meanwhile, different pH values led to different morphologies of powders. When the oxidative decomposition of methyl orange under visible light irradiation is taken into account, both structure and morphology influenced significantly on the photocatalytic activities of powders.

Acknowledgements

We acknowledge the financial support from the Scientific Research Foundation of North China University of Technology (NCUT) and the Natural Science Foundation of Beijing.

References

[1] A. Fujishima, K. Honda, Nature 238 (1972) 37.
[2] Z. Zou, J. Ye, K. Sayama, H. Arakawa, Nature 414 (2001) 625.
[3] J.S. Lee, Catal. Surv. Asia 9 (2005) 217.
[4] J. Yu, A. Kudo, Adv. Funct. Mater. 16 (2006) 2163.
[5] A. Kudo, K. Ueda, H. Kato, I. Mikami, Catal. Lett. 53 (1998) 229.
[6] S. Kohtani, J. Hiro, N. Yamamoto, A. Kudo, K. Tokumura, R. Nakagaki, Catal. Commun. 6 (2005) 185.
[7] L. Zhou, W.Z. Wang, S.W. Liu, L.S. Zhang, H.L. Xu, W. Zhu, J. Mol. Catal. A: Chem. 252 (2006) 120.
[8] S. Tokunaga, H. Kato, A. Kudo, Chem. Mater. 13 (2001) 4624.
[9] S. Kohtani, M. Koshiko, A. Kudo, K. Tokumura, Y. Ishigaki, A. Toriba, K. Hayakawa, R. Nakagaki, Appl. Catal. B: Environ. 46 (2003) 573.
[10] A. Tücks, H.P. Beck, Dyes Pigments 72 (2007) 163.
[11] A.F. Reid, A.E. Ringwood, Earth Planet. Lett. 6 (1969) 205.
[12] A. Kudo, K. Omori, H. Kato, J. Am. Chem. Soc. 121 (1999) 11459.
[13] P. Kubelka, F. Munk, Tech. Z. Phys. 12 (1931) 593.
[14] M.Y. Shin, K.S. Chung, D.W. Hwang, J.S. Chung, Y.G. Kim, J.S. Lee, Langmuir 16 (2000) 1109.
[15] L. Zhou, W. Wang, L. Zhang, H. Xu, W. Zhu, J. Phys. Chem. C 111 (2007) 13659.
[16] R.L. Frost, D.A. Henry, M.L. Weier, W. Martens, J. Raman Spectrosc. 37 (2006) 722.
[17] A. Galembeck, O.L. Alves, Thin Solid Films 365 (2000) 90.
[18] F.D. Hardcastle, I.E. Wachs, J. Phys. Chem. 95 (1991) 5031.
[19] M. Oshikiri, M. Boero, J. Ye, Z. Zou, G. Kido, J. Chem. Phys. 117 (2002) 7313.
[20] J. Tang, Z. Zou, J. Ye, Angew. Chem. Int. Ed. 43 (2004) 4463.
[21] H. Fu, C. Pan, W. Yao, Y. Zhu, J. Phys. Chem. B 109 (2005) 22432.
[22] X. Ling, F. Huang, W. Wang, Z. Shan, J. Shi, Dyes Pigments 78 (2008) 39.